Journal of Nuclear Materials 500 (2018) 349–360

Contents lists available at ScienceDirect

Journal of Nuclear Materials

journal homepage: www.elsevier.com/locate/jnucmat

Effect of the oxidation front penetration on in-clad hydrogen migration

F. Feria*, L.E. Herranz

Unit of Nuclear Safety Research, CIEMAT, Avda. Complutense 40, 28040 Madrid, Spain

HIGHLIGHTS

- A model of in-clad hydrogen migration is derived including oxidation front effect.
- The model is coupled with FRAPCON and assessed through high burnup fuel scenarios.
- The modelling of oxidation front gives rise to hydride rim closer to measurements.

ARTICLE INFO

Article history:
Received 17 September 2017
Received in revised form
17 December 2017
Accepted 8 January 2018
Available online 11 January 2018

Keywords:
Fuel cladding
Hydrogen distribution
Oxidation front

ABSTRACT

In LWR fuel claddings the embrittlement due to hydrogen precipitates (i.e., hydrides) is a degrading mechanism that concerns in nuclear safety, particularly in dry storage. A relevant factor is the radial distribution of the hydrogen absorbed, especially the hydride rim formed. Thus, a reliable assessment of fuel performance should account for hydrogen migration. Based on the current state of modelling of hydrogen dynamics in the cladding, a 1D radial model has been derived and coupled with the FRAPCON code.

The model includes the effect of the oxidation front progression on in-clad hydrogen migration, based on experimental observations found (i.e., dissolution/diffusion/re-precipitation of the hydrogen in the matrix ahead of the oxidation front). A remarkable quantitative impact of this new contribution has been shown by analyzing the hydrogen profile across the cladding of several high burnup fuel scenarios (>60 GW d/tU); other potential contributions like thermodiffusion and diffusion in the hydride phase hardly make any difference. Comparisons against PIE measurements allow concluding that the model accuracy notably increases when the effect of the oxidation front is accounted for in the hydride rim formation. In spite of the promising results, further validation would be needed.

1. Introduction

Fuel safety criteria require keeping the integrity of the cladding as the first barrier to confine the fission products. One of the main cladding degrading mechanism in Light Water Reactors (LWR) fuel is the precipitation of hydrogen picked up during irradiation (i.e., fraction of hydrogen released due to waterside oxidation of the zirconium alloy), which inexorably results in a ductility reduction of the material. Under in-reactor conditions, hydrides formation may foster the cladding failure due to PCMI (Pellet-Cladding Mechanical Interaction) [1,2]; in dry storage, the prevailing conditions may promote the radial reorientation of the hydrides formed, which considerably reduces the cladding ductility [3,4].

A key aspect in the hydrides formation is the distribution of the hydrogen concentration across the zirconium alloy cladding thickness, along with the thermal conditions. The hydrogen that enters the cladding is inhomogeneously distributed throughout the zirconium alloy [4,5]. Indeed, the concentration is much higher close to the cladding waterside, which may result in the so-called hydride rim at high concentrations. Measurements of Elastic Recoil Detection Analysis (ERDA) scans on cross sections of irradiated Zircaloy-4 samples (average burnup of 56 GW d/tU) show hydrogen concentrations in the hydride rim up to 5000 wppm [6]. Given the importance of predicting the hydrogen distribution within the cladding, the migration mechanisms have been studied and modelled [7–11].

First models took into account diffusion and thermodiffusion as

* Corresponding author.
E-mail address: francisco.feria@ciemat.es (F. Feria).

https://doi.org/10.1016/j.jnucmat.2018.01.011
0022-3115/

drivers of the atomic hydrogen migration, and precipitation of zirconium hydrides as a sink of the cited migration [7,8]. Later on, the precipitation kinetics and the hysteresis in the solubility limit have been incorporated in the modelling [9–11]. In spite of the progressive comprehensiveness of models derived so far, they still show limitations in terms of reproducing hydrogen radial profiles observed at high burnup; particularly, predictions result in hydride rim thicknesses significantly lower than values usually measured (50–100 μm or even more [4]), and concentrations well above 5000 wppm.

Models enhancement has been said to require further experimental work to reduce uncertainties in model parameters [10,11]. Nonetheless, it might also be the case that some hydrogen transport mechanisms are still missing in the current modelling. Such a possibility is consistent with experimental findings from which the in-cladding oxidation front displacement may be postulated as a potential driver of hydrogen move deeper in the cladding [12].

The objective of this work is to enhance the predictability of in-cladding hydrogen distribution by proposing a 1D radial model which is based on the current state-of-the-art and includes the oxidation front effect in a simple parametric way. The model, coupled with the FRAPCON code [13], has been used to simulate a number of high burnup fuel scenarios and comparisons to PIE measurements available have been set. Through parametric analyses the quantitative impact of different elements in the model, including the oxidation front move, has been assessed. Therefore, the work presented next might extend the capability of analytical thermo-mechanical tools to estimate the hydrogen distribution in the cladding. This being said, given that some codes use material properties derived from tests performed on prototypical LWR claddings with a hydride rim, the accommodation of such a model would entail a redefinition of material properties.

2. Background

2.1. Phenomenology

During LWRs operation, waterside oxidation of fuel cladding generates hydrogen atoms:

$$Zr + 2H_2O \rightarrow ZrO_2 + 4H$$

Most hydrogen produced is released back to the coolant main stream, but a fraction is absorbed into the cladding (called the hydrogen pickup fraction). The hydrogen is slightly soluble in the α-phase zirconium alloy, so it can either be dissolved in solid solution in the metallic matrix (i.e., hydrogen atoms in interstitial sites) or precipitated as zirconium hydrides, which depends on the Terminal Solid Solubility (TSS) at the prevailing temperature; δ-phase hydrides are mostly formed [14]. Fig. 1 shows the equilibrium binary Zr-H phase diagram; the red lines bound the temperature range of interest (lower bound close to in-reactor coolant inlet temperature [15] and upper bound related to maximum temperature in dry storage [3], which is close to maximum values of in-reactor inner-side cladding temperature [10]).

The hydrogen is redistributed into the metal in response to thermodynamic driving forces [8]. Hydrogen diffuses towards the cladding interior as a result of the concentration gradient set between both sides of the cladding (Fickian diffusion). Nonetheless, the reverse thermal gradient through the cladding causes what is known as thermodiffusion (i.e., Soret Effect), which would mean a slowdown of the net hydrogen motion.

Both hydrogen diffusion and thermodiffusion take place through the metallic matrix. A mass transfer through the hydride precipitates may also happen. However, there is not much driving

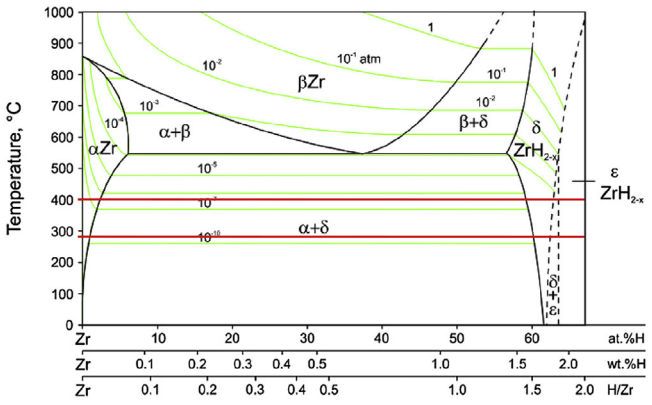

Fig. 1. Equilibrium binary Zr-H diagram [16].

force for diffusion of hydrogen in the δ-phase hydrides [10], given that the hydrogen equilibrium concentration hardly varies in the temperature range of interest; moreover, the diffusivity of hydrogen in hydrides has been measured to be at least 3 times smaller than the diffusivity of hydrogen in zirconium. If the volume fraction of hydride precipitates were not small (i.e. high-burnup fuel), this contribution might not be negligible according to [11].

Concerning the precipitation/dissolution of hydrogen in the zirconium alloy, a hysteresis phenomenon has been observed [17,18]; thus, there is a TSS for dissolution (TSSd) and for precipitation (TSSp). The cause of this hysteresis effect is the volumetric strain related to the difference in densities between the hydrides and the metallic matrix. Additionally, the local stress state in the cladding could cause a significant increase of the solubility limit [10]. Furthermore, precipitation of hydrides was shown to be a non-equilibrium phenomenon at the time scales of interest [19], that is to say, the hydrides formation is a transient process between a non-equilibrated initial condition and the final steady state equilibrium. Concerning the dissolution of hydrides, the rate of dissolution is assumed to be much faster than the rate of precipitation and equilibrium is approached [9,10].

One issue of interest during the cladding oxidation process is the behavior of the hydrogen coming from hydrides when the oxidation front moves inward by transforming the hydrided phase in oxide [12]. The assumptions formulated are:

- Dissolution/diffusion/re-precipitation of the hydrogen in the matrix ahead of the oxidation front.
- Trapping in the oxide.
- Release in the environment.

Based on corrosion tests on hydrided Zircaloy-4 samples [12], it was observed that the hydrogen initially present in the hydrided matrix was not incorporated in the oxide, being mainly pushed ahead of the oxidation front. Fig. 2 shows a conceptual representation of the phenomenon observed (it is assumed that the hydrogen dissolved is also incorporated in the metallic matrix). Additionally, the cladding thinning due to corrosion increases the cladding stress and the temperature gradient, which could affect the hydrogen migration. Thus, the hydrogen distribution may be altered when the oxidation front moves forward.

2.2. Modelling

The modelling status concerning hydrogen transport within the cladding has been recently described [10,11] and implemented in the BISON and SVECHA/QUENCH codes. It is worth noting that none

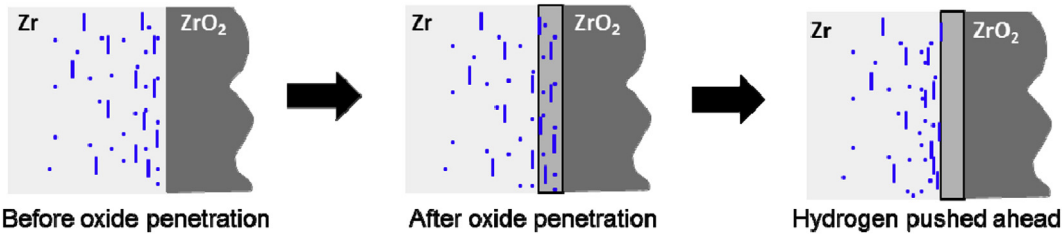

Fig. 2. Scheme of oxidation front effect on hydrogen in the cladding (blue lines represent hydrogen precipitates, H_p, and blue dots represent dissolved hydrogen, H_d). (For interpretation of the references to colour in this figure legend, the reader is referred to the Web version of this article.)

of them includes the above mentioned effect of the oxidation front (i.e., dissolution/diffusion/re-precipitation of the hydrogen present in the matrix converted in oxide).

The general equation used to model the migration of hydrogen is based on the Fick's second law. Focusing on the radial direction, r, the evolution of the hydrogen concentration, H, can be expressed as:

$$\frac{\partial H}{\partial t} = -\frac{\partial H}{\partial r} \tag{1}$$

with J the hydrogen flux. Both H and J encompass the contribution of the dissolved and precipitated phases in the metal matrix (expressed through sub-indexes d and p, respectively):

$$H = H_d + H_p \tag{2}$$

$$J = J_d + J_p \tag{3}$$

In order to consider the mass transfer through a two phase-region, the volume fraction of the hydride phase, f, is accounted for. It is determined through the ratio between H_p and the local concentration of hydrogen in hydride precipitates, H_δ, which is approximated in two ways:

- A constant amount obtained from the molecular weights [10].
- From the equilibrium binary Zr-H phase diagram shown in Fig. 1 [11].

Thus, equations (2) and (3) can take the form:

$$H = H_{zr}\cdot(1-f) + H_\delta \cdot f \tag{4}$$

$$J = J_{zr}\cdot(1-f) + J_\delta \cdot f \tag{5}$$

with H_{zr} the local concentration of hydrogen in the α-phase zirconium alloy. The hydrogen flux in each phase is obtained by the sum of the Fickian diffusion term and the thermodiffusion term:

$$J_i = -D_i\left(\frac{\partial H_i}{\partial r} + \frac{Q_i^* H_i}{RT^2}\frac{\partial T}{\partial r}\right), i = zr,\delta \tag{6}$$

where T is the temperature, D_i is the diffusion coefficient of hydrogen and Q^*_i is the heat of transport in the temperature gradient. The sub-index i indicates α-zirconium phase (zr) or δ-hydride phase (δ).

The diffusion of hydrogen in the δ phase is neglected in Ref. [10], based on the considerations previously mentioned. Instead, this effect is considered in Ref. [11], based on the fact that the volume fraction of hydride precipitates is large enough at high burnup.

The calculation of the precipitation rate is based on the linear approximation in the hydride precipitation model [8,14]; concretely, the rate of precipitation was measured to be proportional to the hydrogen supersaturation. If the concentration in solid solution lies between TSS_d and TSS_p (i.e., hysteresis area), neither dissolution nor precipitation occurs. When the concentration in solid solution is below TSS_d, the hydrides (if they are present) are assumed to be dissolved at a rate proportional to the hydrogen undersaturation. Thus, the precipitation/dissolution rates are determined from TSS (i.e., TSS_p and TSS_d) and the precipitation and dissolution rate parameters (k_p and k_d, respectively):

$$\frac{\partial H_p}{\partial t} = \begin{cases} k_p\cdot(H_{zr} - TSS_p)\cdot(1-f) & \text{if } H_{zr} > TSS_p \\ 0 \text{ if } TSS_p \geq H_{zr} > TSS_d \\ k_d\cdot(H_{zr} - TSS_d)\cdot(1-f) \text{ if } H_{zr} \leq TSS_d \text{ and } H_p > 0 \\ 0 \text{ if } H_{zr} \leq TSS_d \text{ and } H_p = 0 \end{cases} \tag{7}$$

The model parameters D_i, TSS_p, TSS_d and k_p are estimated through an Arrhenius' equation:

$$\text{Parameter} = A\cdot\exp\left(-\frac{B}{R\cdot T}\right) \tag{8}$$

with A and B fitting parameters obtained from experimental data, and R the ideal gas constant (8.31 J/mol/K). Q^*_i and k_d are assumed to be constant; whereas the heat of transport is experimentally determined, the dissolution kinetics is usually assumed to be very fast compared to precipitation kinetics, as previously mentioned. The parameters used in Refs. [10] and [11] come from unirradiated material tests [7,8,19]. Indeed, very few irradiated data are available.

Concerning the boundary conditions for the hydrogen flux, models usually assume a constant pickup fraction of all the hydrogen being produced by the oxidation reaction; such a fraction depends on the zirconium alloy and it usually ranges from 10 to 20%.

High burnup fuel simulations carried out with the modelling shown [10,11] gave rise to predictions of thin hydride rim (around 50 μm or even less) with high hydrogen concentration (around 10000 wppm or even more). Although the data measured so far on high burnup fuel show discrepancies in the rim formation [11], thicker hydride rims with considerably less hydrogen concentration than predicted were observed, as previously cited.

The potential source of the discrepancies found was investigated. It was shown that an important reduction of k_p (i.e., few orders of magnitude) would help to enhance the predictions accuracy, which might be justified by the influence of irradiation on the precipitation rate [11]. According to [10] a non-uniform heat of transport or the effect of stress on TSS_p have the most potential for helping to predict the experimental observations. No conclusive statement can be made and further investigation was recommended both from separated effect tests to account for the cited phenomena and from irradiated rods to soundly validate the modelling.

3. Methodology

3.1. 1D model

In this work, the radial transport of hydrogen throughout the cladding thickness has been modelled based on equations (1)–(8). A zero hydrogen flux has been imposed at the clad inner side, whereas at the outer one the hydrogen pickup fraction has been provided according to what is coded in FRAPCON [13] (coupling explained below). The mass transfer related to this hydrogen pickup has been modelled by directly increasing the hydrogen dissolved in the metallic matrix.

The oxidation front effect has been also modelled as an additional contribution. To do that, the cladding thinning due to corrosion has been expressed through the equation:

$$dr_{ox} = \frac{\delta_{ox}}{PB} \tag{9}$$

with dr_{ox} the thickness of the initial cladding which has been converted in oxide, δ_{ox} the oxide thickness and PB the Pilling-Bedworth ratio for zirconium oxide (1.56). The calculated cladding thinning has been accounted for in the temperature gradient estimation.

The effect of the dissolution/diffusion/re-precipitation of the hydrogen in the material ahead of the oxidation front is modelled based on the following assumptions:

- Dissolution/diffusion are instantaneous (i.e., much faster than any other process involved).
- Re-precipitation kinetics depends on the phase ahead of the oxidation front. A hydride phase would favor nucleation and the process is considered instantaneous, whereas in α-zirconium re-precipitation follows the same kinetics as precipitation.
- All hydrogen reached by the oxidation front is pushed ahead of it (i.e., no absorbed hydrogen is ever lost from cladding). Any deviation from this "perfect sink" assumption might be accommodated through the hydrogen pickup fraction that is provided as a boundary condition of the model. It is assumed that the hydrogen pickup fraction of the fuel performance code used (i.e., FRAPCON) does not have to be modified, based on the fact that the supporting experimental database should implicitly include this effect (observed in Ref. [12], as previously mentioned).

Accordingly, the precipitation rate is re-casted as,

$$\frac{\partial H}{\partial t} = \frac{\partial H_{p0}}{\partial t} - rp \cdot \frac{\partial H_{ox}}{\partial t} \tag{10}$$

where H_{p0} is the precipitated hydrogen obtained from equation (7) (i.e., based on previous modelling), H_{ox} is the concentration of precipitated hydrogen covered by the oxidation front, and rp is the fraction of H_{ox} that does not re-precipitate instantaneously (the re-precipitation kinetics has been modelled by the same k_p as the precipitation). In previous models, since the effect of the oxidation front is not accounted for, it is equivalent to assume that all the hydrides covered by the oxide layer re-precipitate instantaneously.

It should be noted that the modelling of the cladding thinning due to oxide penetration (i.e., volume reduction) and the hydrogen "push ahead" effect, entail an increase of the hydrogen concentration additional to the direct hydrogen uptake. According to equation (10), the hydrides corresponding to H_{ox} remain as they are if rp is null (i.e., instantaneous re-precipitation of all of them), while a fraction of H_{ox} is dissolved, with the consequent re-precipitation along time, if rp is greater than zero.

The model derived has the option to choose between different models parameters found in the literature for zircaloy material (mainly Zircaloy-4) and valid under representative temperatures in the range 280–400 °C (some exception shown below). In Table 1 parameters needed in the model are displayed according to two different options, default and optional. Overall, "default" means values traditionally used whereas "optional" refers to new values published. By using these options one might derive the variability of the model depending on in-model parameters setting. As it is pointed out the oxidation front effect is not considered by default (i.e., $f_{ox} = 0$); when this contribution is activated (i.e., $f_{ox} = 1$) a value for the parameter rp should be introduced in the input.

From Table 1 several aspects should be noted:

- The alternative solubility limits found are supported on data from unirradiated and irradiated Zircaloy-2 samples, based on experimental observations that show no significant impact of the irradiation [18].
- The parameter k_p used by default increases with temperature up to 352 °C, above which the rate is clamped at this maximum temperature based on experimental observations [10]; regarding the optional k_p, a constant value is assumed in Ref. [14], given that only a slight dependence on temperature was measured, in contrast with previous studies.
- H_δ by default is considered as the hydrogen concentration in the α-δ, δ phase boundary according to [20]; it has been approximated by a polynomial fitting within the range of temperatures of interest (from Fig. 1):

$$H_\delta = A + B \cdot T^2 \tag{11}$$

Fig. 3 shows the differences between options in the case of TSS and k_p. There is a wider validity range in the optional parameters, in particular, the TSS_p by default does not cover representative conditions, so an extrapolation should be assumed. Moreover, the optional parameters are greater than by default, except k_p above 348 °C, where there is small differences. The difference between the options of k_p is particularly large at low temperatures (i.e. close to 280 °C). In the case of TSS, the hysteresis area is much larger in the optional case.

The model derived is solved by the numeric method of finite differences. To do that, the time step, Δt, and the number of radial nodes throughout the cladding thickness, N, are defined as inputs of the model, as well as the initial conditions (i.e., as-fabricated cladding thickness, th, and initial hydrogen concentration, H_i) and the end time, t_{end}. Regarding the boundary conditions (i.e., hydrogen pickup, H_{pk}, oxide thickness and thermal conditions), the model has been adapted to account for them both through the input and by the coupling with a fuel performance code. Fig. 4 shows the flow chart of the model.

3.2. Coupling

In order to feed the model derived with proper boundary conditions, it has been coupled with FRAPCON (version 4.0) [13]. The coupling has been based on the post-processing of the FRAPCON computation with the 1D model. Although this work has been focused on in-reactor conditions, the model has been also coupled with the FRAPCON extension to dry storage carried out by CIEMAT, called FRAPCON-xt [23].

As previously mentioned, the hydrogen pickup provided by FRAPCON is used as the boundary condition in the waterside node (in the fuel side node a null hydrogen flux is imposed). The oxide thickness given by the code is used for the above mentioned oxidation front modelling. Concerning the thermal conditions,

Table 1
Model parameters.

Parameter	Default		Reference	Optional		Reference
	A	B		A	B	
D_{zr} (m^2/s) [a]	$0.8 \cdot 10^{-7}$	33306	[19]	–	–	–
D_δ (m^2/s) [a or b]	$1.3 \cdot 10^{-7}$	53131	[21]	0	–	Approach
TSS_p (wppm) [a]	$1.4 \cdot 10^5$	34470	[17]	$0.3 \cdot 10^5$	25042	[18]
TSS_d (wppm) [a]	$1.1 \cdot 10^5$	35991	[17]	$1.4 \cdot 10^5$	36686	[18]
k_p (s^{-1}) [a or b]	3881	82400	[19]	$4.5 \cdot 10^{-4}$	–	[14]
k_d (s^{-1}) [b]	1	–	Approach	–	–	–
Q^*_{zr} (J/mol) [b]	25070	-	[19]	30000	–	[22]
Q^*_δ (J/mol) [b]	5430	–	[20]	0	–	Approach
H_δ (wppm) [c or b]	17200	$-5.2 \cdot 10^{-3}$	Fitting from Fig. 1	17872	–	[10]
f_{ox} [d]	0	–	–	1	–	–
rp [b]	–	–	–	$0 \leq A \leq 1$	–	Approach

[a] Defined by equation (8).
[b] Constant value.
[c] Defined by equation (11).
[d] Factor to deactivate (0)/activate (1) the oxidation front contribution.

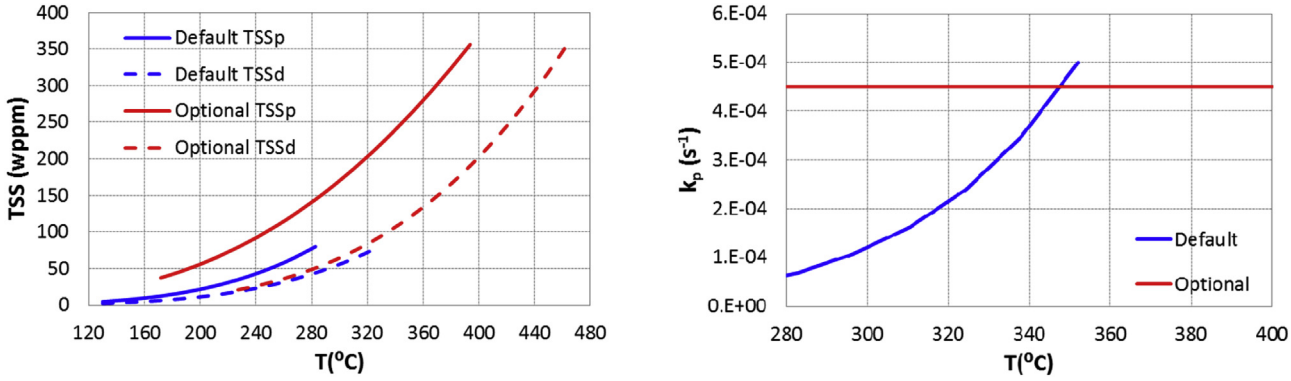

Fig. 3. Solubility limits (plot on the left) and precipitation rate parameter (plot on the right) as a function of temperature (within their validity range).

FRAPCON calculates the inner and outer cladding temperature (T_{in} and T_{out}, respectively), so the model derived uses these values to estimate the thermal gradient in the nodes established; to do that, a linear interpolation is assumed as a good approximation. Note that FRAPCON thermal calculations account for the cladding thinning due to corrosion. Fig. 5 illustrates the coupling accomplished.

It should be noted that the output of FRAPCON provides the average hydrogen concentration within the cladding. Therefore, the above explained coupling with the model derived allows extending the prediction to the detailed radial profile of hydrogen concentration.

4. Assessment

4.1. Out-of-pile scenario

The out-of-pile database available is scarce and the tests included are not completely representative of the target scenario. In most cases there is neither oxidation nor hydrogen flux at any boundary, and temperature gradient and dimensions of the samples are not appropriate either.

Nonetheless, by using data from Ref. [7] a qualitative model-to-data comparison has been set. In the experiment chosen a Zircaloy-2 cylinder of 2.5 cm in length (1.2 cm in diameter) was uniformly pre-charged with a hydrogen concentration of 130 wppm. It was annealed for 34 days under a temperature gradient with hot and cold ends at 477 °C and 130 °C, respectively. According to these conditions, thermodiffusion was an important contribution to hydrogen migration in this case.

Model simulations have been performed with parameters by default and by checking each alternative option provided in Table 1. Note that an extrapolation out of the validity range of most of the parameters had to be assumed, given the prevailing thermal conditions of the test. Since there was not oxidation during the experiment, the f_{ox} default value (0) has been chosen. The initial and boundary conditions have been introduced through the input (without hydrogen pickup). The time step and the number of radial nodes applied have been 1 s and 200, respectively.

Average relative deviations, RDs, lower than 1% have been obtained when the parameters D_δ, Q^*_δ and H_δ are moved from the default option, which is due to the relatively low concentration of hydrides in this experiment.

Figs. 6 and 7 represent those parametric cases that show the highest impact with respect to the default case. Fig. 6 depicts the results obtained by varying Q^*_{zr}, k_p and TSSs (i.e., TSS_p and TSS_d) in different runs. The estimation obtained by previous modelling [10] is also included; as expected, it is nearly identical to the one of the default case.

As observed from Fig. 6, all the estimates match data at lengths over 1 cm. Between 0 and 1 cm, all the simulations look qualitatively consistent with measurements, with no drastic differences among them. Even though a maximum hydrogen concentration is predicted between 0.5 and 0.8 cm in all calculations (data maximum was located at around 0.6 cm), none was capable to reach the experimental maximum value (around 550 ppm), remaining about 100 ppm below that value. As expected, the

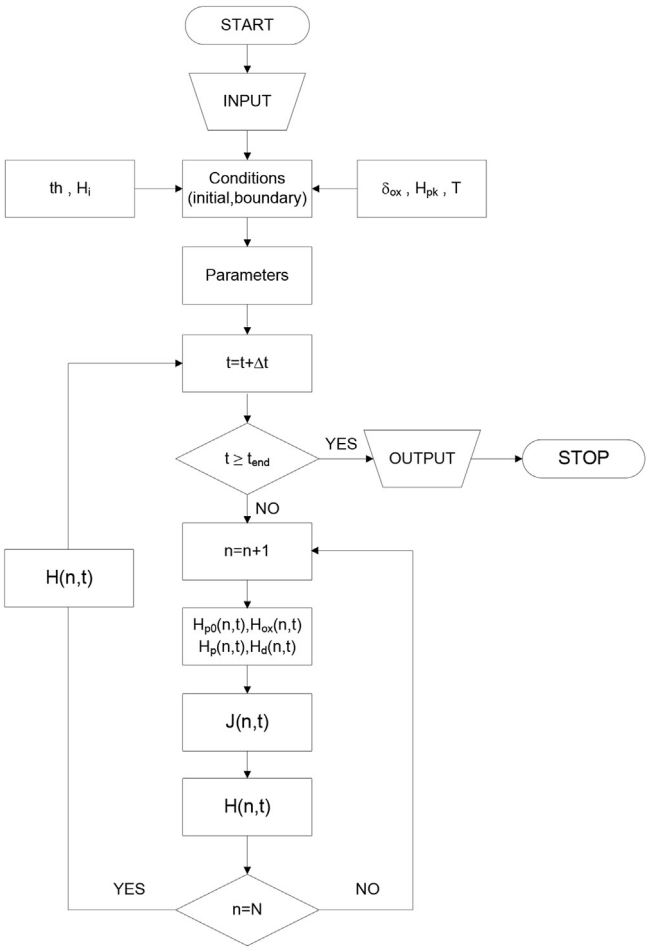

Fig. 4. Flow chart of the model.

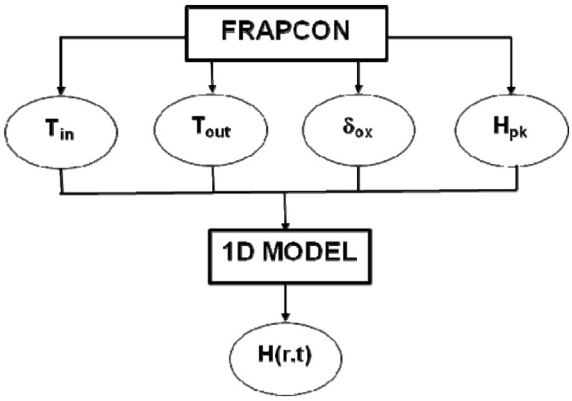

Fig. 5. Model coupling with FRAPCON.

greater Q^*_{zr}, the greater the hydrogen concentration transported to the cold end. In the case of k_p, the faster kinetics gives rise to a higher hydrogen accumulation in the cold end. RDs lower than 15% are obtained in both cases. Concerning TSSs, the higher solubility allows more dissolved hydrogen to be transported to the cold end; in this case, greater RD is obtained (around 30%).

In spite of not obtaining a substantial enhancement, the alternative parameters seem to help the model to better capture the experimental trend observed. However, only the synergy between

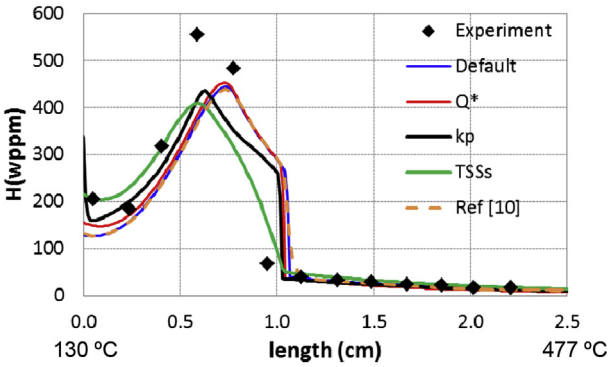

Fig. 6. Model-to-data comparison by using parameters by default and alternative options. Results shown in Ref. [10] included.

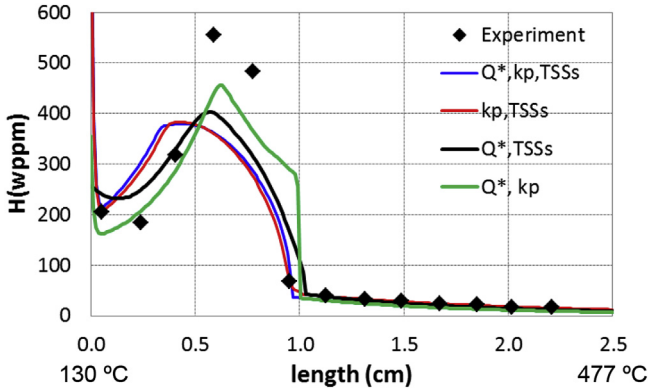

Fig. 7. Model-to-data comparison by using combinations of optional parameters.

Q^*_{zr} and k_p has given rise to better predictions (Fig. 7), which may be due to the fact that optional TSSs (based on irradiated and unirradiated data, as mentioned above) are not totally appropriate for the material tested in the experiment considered (i.e., unirradiated material). Overall, the model seems to be well formulated according with its capability to qualitatively reproduce the measured profile, both with its default and optional parameters. Nevertheless, more data, more representative, are needed to validate the model and recommend the best estimate parameters.

4.2. In-pile scenario

4.2.1. Hypothetical

A postulated scenario of irradiated fuel rod has been simulated to assess the model from a qualitative point of view. It is a typical 17 × 17 PWR fuel rod irradiated to an average burnup of 65 GW d/tU. Rod design and power history are detailed elsewhere [15].

FRAPCON predictions from two axial nodes of the upper part of the fuel rod (called ax1 and ax2) have been provided to the model in order to obtain different cases of hydrogen distribution. Fig. 8 shows the power history simulated (i.e., evolution of the average linear power, q'), as well as the evolution predicted of the inner and outer temperatures, the oxide thickness and the hydrogen pickup.

Model simulations have been done with the input data shown in Table 2. The initial hydrogen concentration commonly used by FRAPCON [13] has been applied. The variable t_{end} corresponds to the in-reactor end-of-life (EOL), at which the hydrogen picked up is 632.5 wppm and 1093.3 wppm for ax1 and ax2, respectively (80.8 μm and 136.5 μm for the oxide thickness).

The model parameters by default have been used as the base

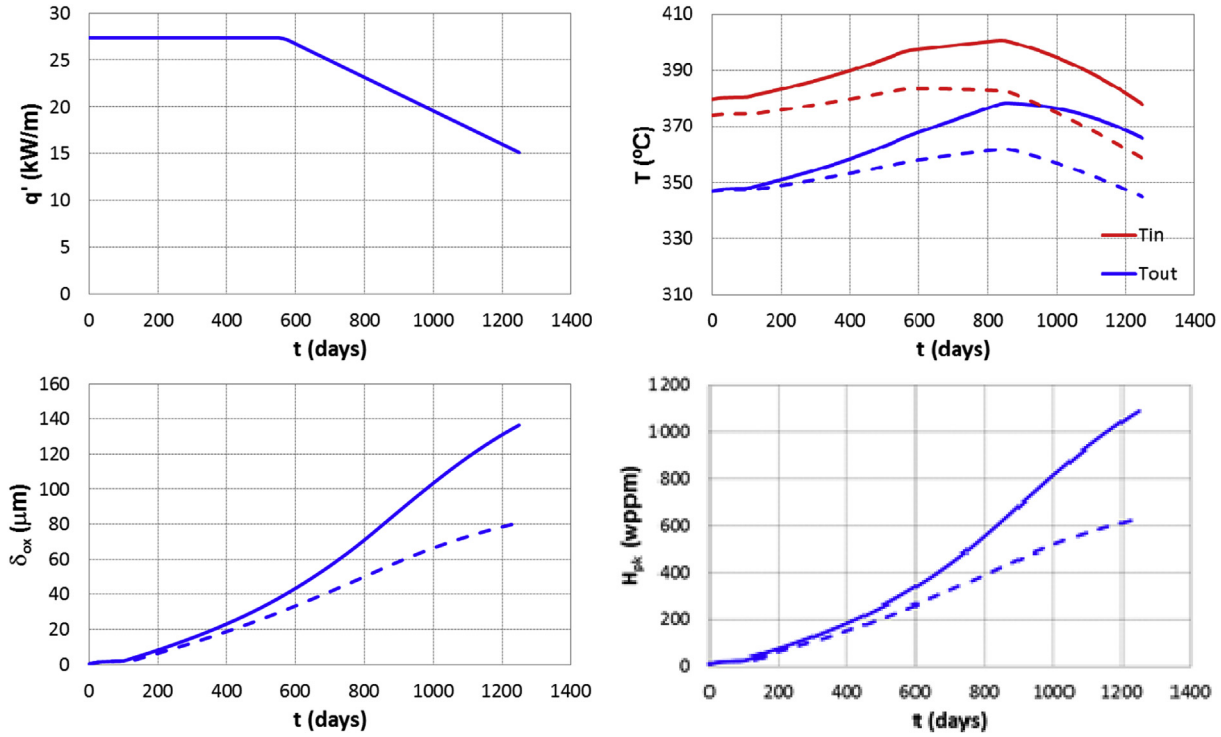

Fig. 8. Power history and model boundary conditions for ax1 (dashed line) and ax2 (continuous line).

Table 2
Model input data for ax1 and ax2.

Variable	Value
Δt (s)	1
N	20
th (μm)	610
H_i (wppm)	10
t_{end} (days)	1249

case to assess the impact of the alternative parameters shown in Table 1. An additional parametric case to study the influence of the thermodiffusion contribution has been performed (i.e., $Q^*_{zr} = 0$). Figs. 9–11 depict the base case results and the comparison with the parametric cases in terms of the EOL hydrogen radial distribution (the radial coordinate is shown with the cladding inner radius, r_{in}, subtracted, and normalized to the EOL thickness). Overall, the calculations indicate a two region cladding in between which a large hydrogen gradient is set. The following observations have been made from the predictions without the modelling of the oxidation front effect (Figs. 9 and 10 for ax1 and ax2, respectively):

- By comparing ax1 and ax2 predictions it is noted that the higher the hydrogen uptake, the thicker the hydride rim. In both cases high hydrogen concentrations are predicted in the most outer region of the cladding (around 9600 wppm in ax1, and an average of 9100 wppm with a peak of 14900 wppm close to the waterside in ax2), and once out of the hydride rim a sharp hydrogen concentration reduction to levels around 150–220 wppm is estimated. It is worth noting that the rim thickness is predicted to be smaller than 60 μm.
- The impact of the thermodiffusion contribution is not important (shown in Fig. 9a, b, 10a and 10b).
- Even at high concentrations of hydrogen absorbed, the hydrogen transport in the hydride phase hardly affects the hydrogen profile predicted, as shown in Figs. 9e and 10e.
- The effect of the optional precipitation rate parameter is negligible (shown in Figs. 9c and 10c).
- The alternative option of TSSs shows important deviations with respect to the base case according to Figs. 9d and 10d (RD of 40%, approximately). Concretely, lower hydrogen concentrations in the hydride rim are predicted (around 8100 wppm in ax1, and an average of 8400 wppm with a peak of 14800 wppm close to the waterside in ax2), which gives rise to higher concentrations below the rim (up to 300 wppm). Indeed, the higher TSS_s, the higher the concentration gradient of dissolved hydrogen.
- The optional H_δ hardly affects the hydrogen profile predicted in ax1 (Fig. 9f). Instead, it has given rise to noticeable deviations in the hydride rim of ax2 (RD of around 40%), as shown in Fig. 10f. According to these results, it seems that the concentration of the hydrides formed in ax1 is not high enough to give rise to a noticeable impact of H_δ variability. In the case of ax2, the higher H_δ, the higher the maximum concentration attained in the outer part of the cladding (17000 wppm, approximately), due to a lower hydride volume fraction (i.e., larger zirconium matrix, so lower local concentration of dissolved hydrogen and less concentration gradient).

When the oxidation front effect is activated, the main observations are (Fig. 11):

- The hydrogen distribution profiles are practically the same as in the case by default if instantaneous re-precipitation is assumed (i.e., rp = 0) (Fig. 11a and b). This means a negligible effect of the variation in the temperature gradient due to the cladding thinning as a consequence of the corrosion (thickness reduction of 51.7 μm in ax1 and 87.4 μm in ax2, which gives rise to temperature gradient increase of around 10% and 15%, respectively).

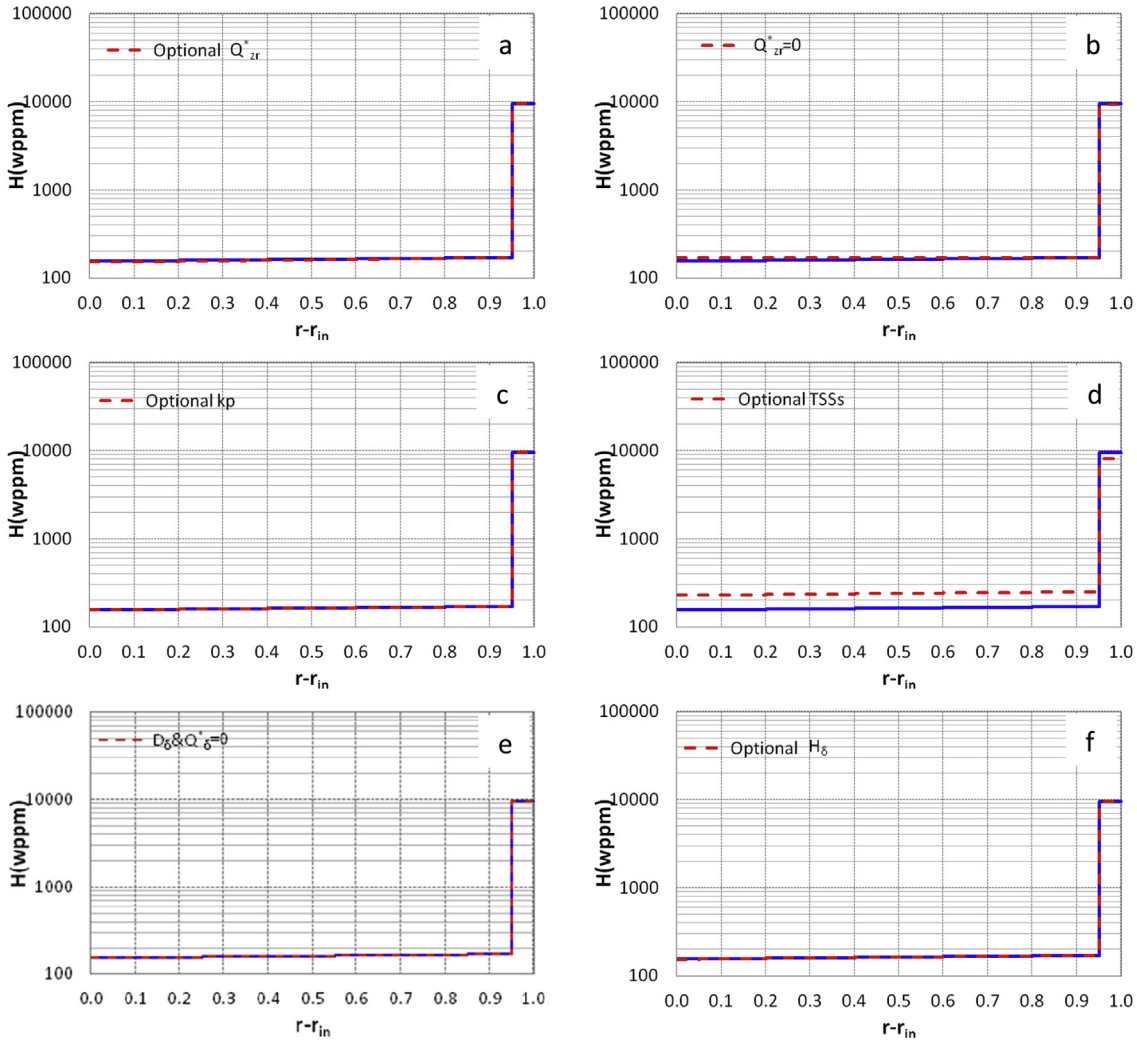

Fig. 9. EOL hydrogen radial distribution (radius normalized) for ax1: case by default (blue line) and parametric cases without oxidation front effect (red dashed line). (For interpretation of the references to colour in this figure legend, the reader is referred to the Web version of this article.)

- Deviations with respect to the default case can be observed from rp values of 0.5, being significant from 0.8 (Fig. 11c and d); the trend is to reduce the hydrogen concentration in the hydride rim and to enlarge the rim thickness.
- A non-expected hydrogen profile is obtained close to the waterside when there is not any fraction of instantaneous re-precipitation (i.e., rp = 1) (Fig. 11e and f). Indeed, experimental observations show a nearly constant high hydrogen concentration at the outer layer facing the coolant [4].

Additional parametric cases have been conducted to determine the maximum rp value (rp_{max}) that would give rise to profiles qualitatively consistent with observations [4] (i.e., a nearly constant high hydrogen concentration at the outer layer facing the coolant and a jump down to much lower hydrogen contents when moving inward from such a layer). The results indicate that just a small fraction of hydrogen instantaneously re-precipitated would be needed (2.5% for ax1 and 2% for ax2) to match the profile described. As observed in Fig. 12, modelling the oxidation front effect results in thicker hydride rims with lower hydrogen concentrations (reduction of 50%, approximately).

It should be noted that the predicted profiles convey a similar message: most of hydrogen absorbed remains in the outer clad region with hydrogen concentrations reaching much higher levels than rough averages. Such information might be highly relevant to model both in-reactor transients and long-term dry storage.

4.2.2. Irradiated rod

A sound model validation against irradiated fuel data would require a wide dataset of post irradiation examination (PIE) measurements of hydrogen radial distribution, along with the corresponding rod design and irradiation conditions. In most of the cases this information is not available.

In this work, a model-to-data comparison has been performed based on PIE measurements from a 17 × 17 PWR fuel rod clad with ZIRLO and irradiated for 5-cycles (average burnup of about 69 GW d/tU) [24]. Particularly, measurements from two axial positions of the upper half of the fuel rod (fuel fissile height of 3658 mm) have been gathered (called v1 and v2). Measurements were performed at specific radial positions across the cladding wall based on Scanning Electron Microscopy (SEM) images; the hydrogen concentration was calculated from the area fraction of hydrides in each image.

Table 3 shows the main characteristics of the cases v1 and v2. As it can be observed, although very similar oxide thicknesses were measured, the measurements of hydrogen concentration were

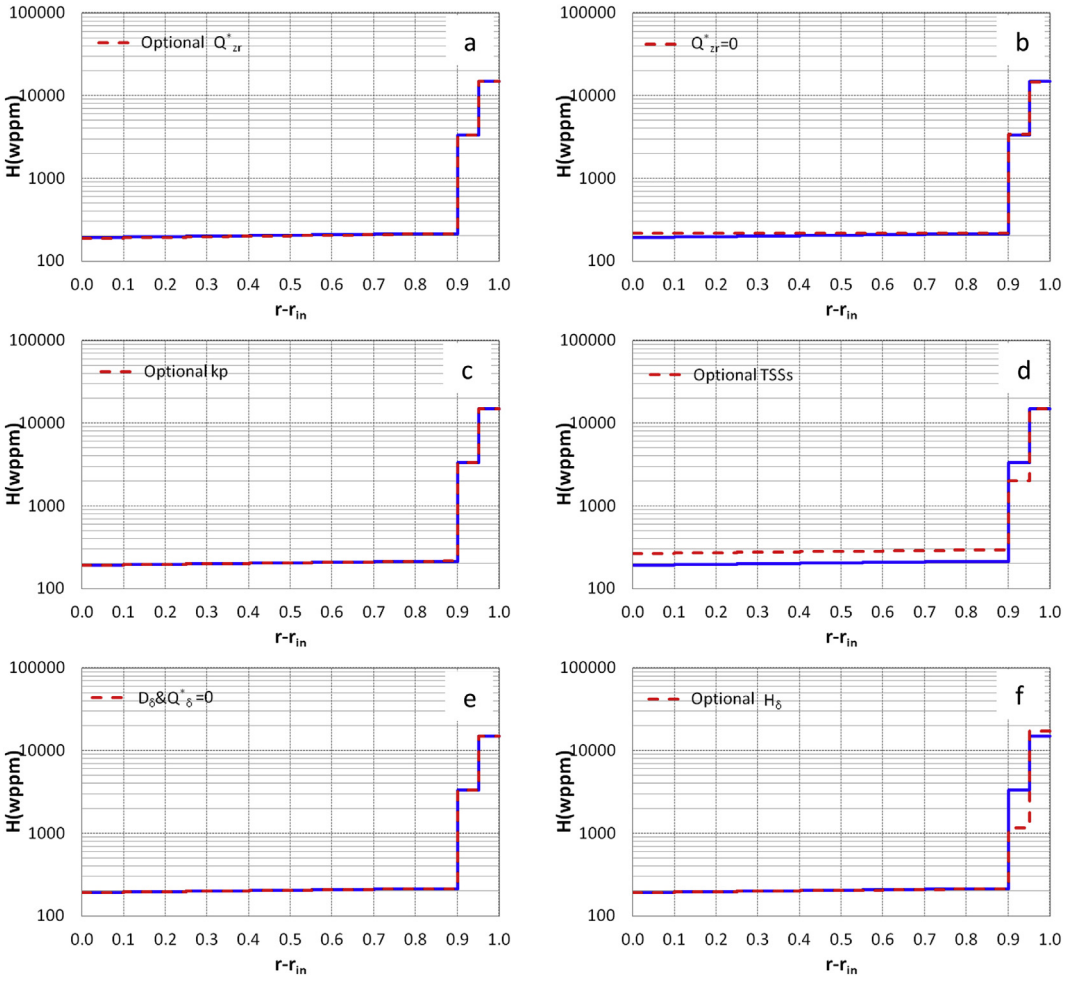

Fig. 10. EOL hydrogen radial distribution (radius normalized) for ax2: case by default (blue line) and parametric cases without oxidation front effect (red dashed line). (For interpretation of the references to colour in this figure legend, the reader is referred to the Web version of this article.)

quite different.

FRAPCON simulations have been itted to the δ_{ox} and H_{pk} values shown in Table 3, in order to accomplish a meaningful comparison against data. To do so, the oxidation rate and the hydrogen pickup fraction have been modified in the source code. Fig. 13 illustrates the power history simulated with FRAPCON, and the results obtained along the irradiation period in terms of the inner and outer temperatures, the oxide thickness and the hydrogen picked up. The thermal predictions are practically the same for both cases, given the proximity of the axial positions.

The model has been run with the boundary conditions shown (Fig. 13). Table 4 shows model input data used, where t_{end} corresponds to EOL time. According to the choice of the model parameters (Table 1), two types of cases have been run: default and optional (i.e., all the optional parameters have been chosen, as well as a zero value of rp). In both cases, parametric studies have been made to find rp_{max} (in the default case, f_{ox} has been changed to 1). Note that the model parameters from Table 1 have been assumed to be valid for ZIRLO, given the lack of this kind of information for this material.

Figs. 14 and 15 show the model-to-data comparison for each case studied. The hydride rim in each measured profile is assumed to be the outer section of 93 μm with high hydrogen concentration (i.e., 4405 wppm in v1 and 6595 wppm in v2). In the matrix below the hydride rim, although the central zone seems to be well predicted (especially in the default cases, independently of the oxidation front modelling), the measurements close to the fuel side and to the hydride rim are not well captured by the predictions, especially in the inner part where a clear overprediction is obtained.

From the hydride rim comparison when the oxidation front is not modelled, it can be pointed out:

- Notable overpredictions of the hydrogen concentration, with relative errors, RE, greater than 100%. The lower the hydrogen absorbed, the greater the discrepancies (i.e., RE from 127% to 204% in the default case, and from 165% to 182% in the optional case). The optional case reduces RE in v1 mainly due to the above mentioned effect of the higher TSSs. The contrary trend is observed in v2, due to the effect of H_δ at high concentrations of hydrogen absorbed (previously explained).
- Important underpredictions of the rim thickness, with minimum RE of around 40%. The higher the hydrogen absorbed, the lower RE, as expected according to the results in the previous section. The predictions are independent of the model parameters choice.

It should be highlighted that the modelling of the oxidation front with rp_{max} notably reduces the discrepancies found in the hydrogen concentration of the hydride rim (RE of about 30%). The

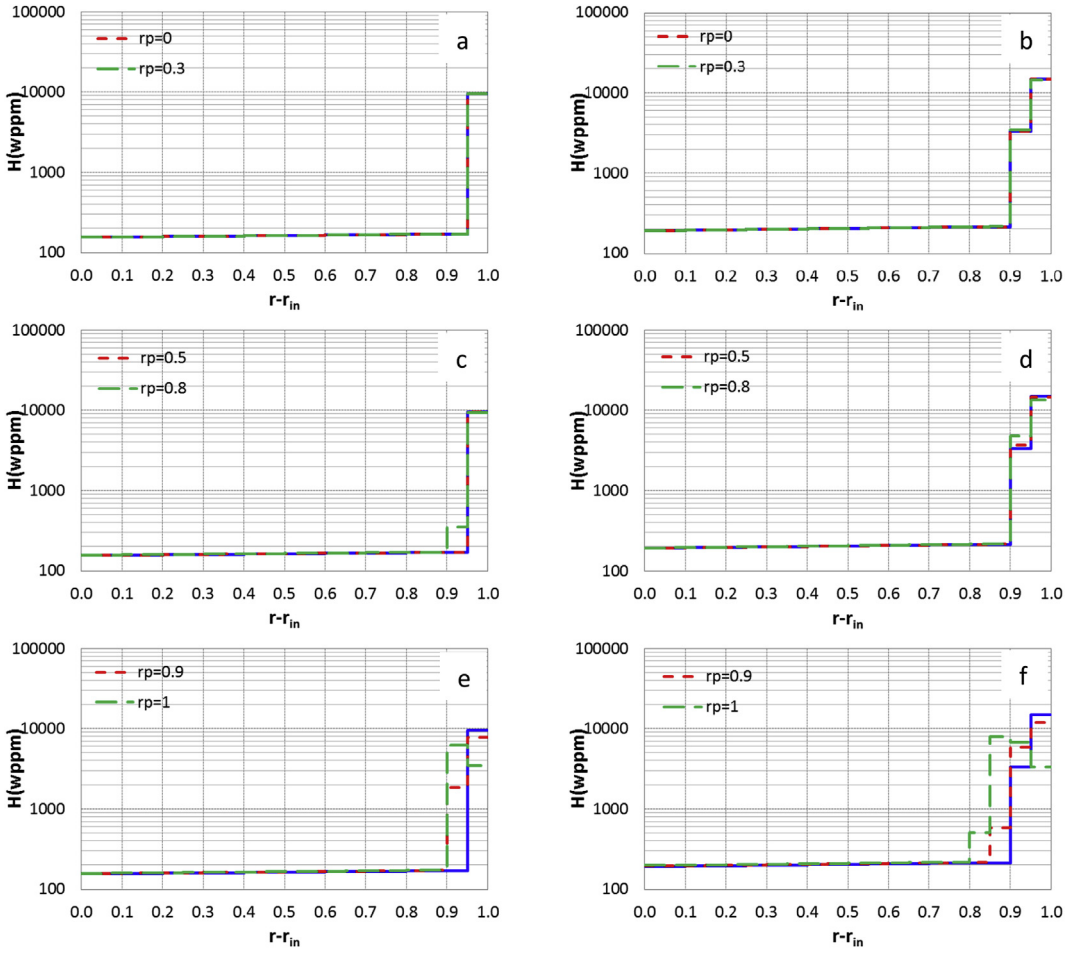

Fig. 11. EOL hydrogen radial distribution (radius normalized) for ax1 (plots on the left) and ax2 (plots on the right): case by default (blue line) and parametric cases with oxidation front effect and different rp (dashed lines). (For interpretation of the references to colour in this figure legend, the reader is referred to the Web version of this article.)

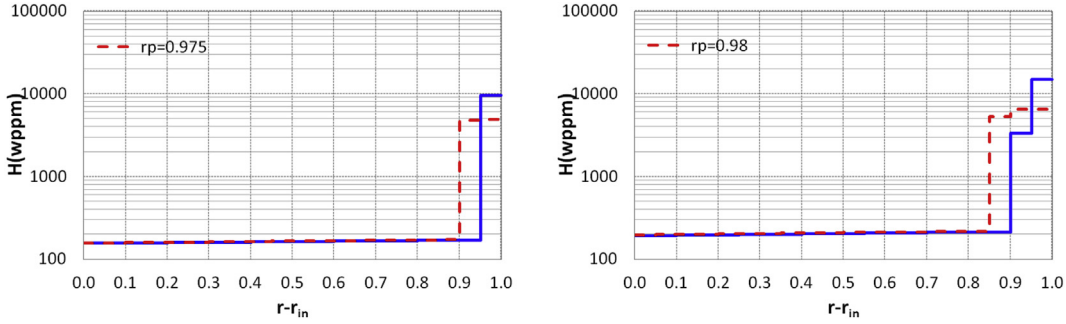

Fig. 12. EOL hydrogen radial distribution (radius normalized) for ax1 (plots on the left) and ax2 (plots on the right): case by default (blue line) and parametric case with oxidation front effect and rp_{max} (red dashed line). (For interpretation of the references to colour in this figure legend, the reader is referred to the Web version of this article.)

Table 3
Characteristics of validation cases.

Variable	v1	v2
Axial position (mm)	2924	2925.5
Azimuth (°)	0	0
δ_{ox} (μm)	104	103
H_{pk} (wppm)*	926	1280

* Averaged through the cladding wall.

relative error in the rim thickness is also reduced to values of roughly 18%. As in the postulated scenario, rp_{max} corresponds to a small fraction of instantaneous re-precipitation (around 2.5%).

In spite of the promising results when the oxidation front is accounted for, further validation should be done with a sounder database (i.e., more measured profiles with local measurements in smaller sections close to the waterside), more representative of high burnup fuel discharged (i.e., hydrogen pickup limited to 600 wppm [2]). Moreover, more data about the oxidation front effect would be needed for a sounder modelling.

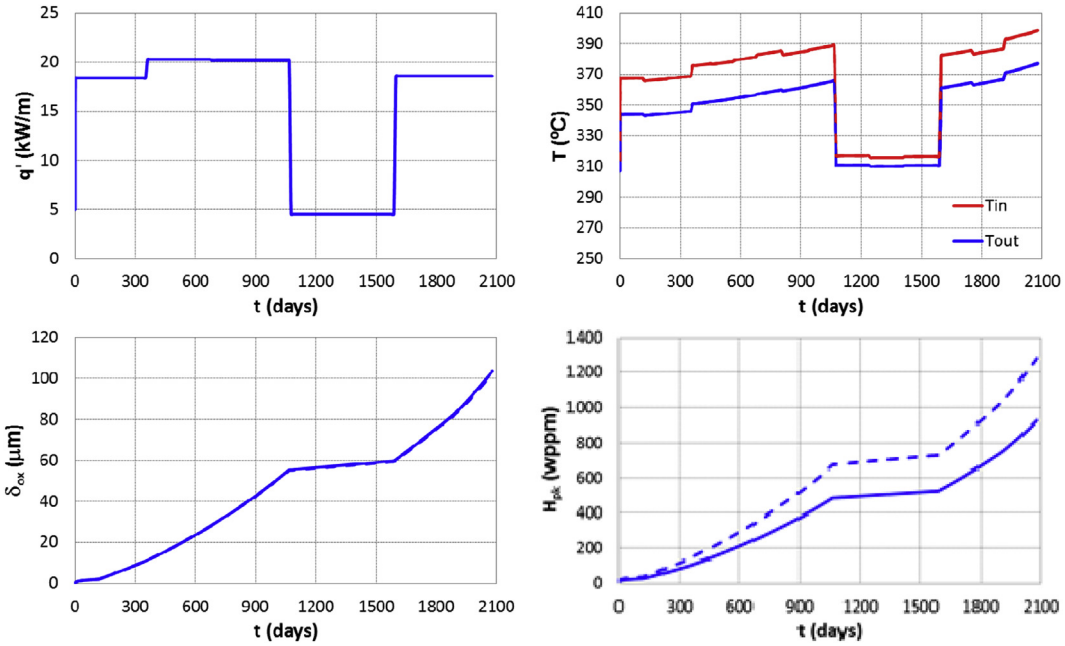

Fig. 13. Power history and boundary conditions for the validation cases represented by continuous line (v1) and dashed line (v2).

Table 4
Model input data for the validation cases.

Variable	Value
Δt (s)	1
N	20
th (μm)	572
H_i (wppm)	10
t_{end} (days)	2078

5. Conclusions

In the present work, the hydrogen radial migration within the cladding has been modelled and coupled with FRAPCON. In order to obtain a comprehensive model, the state-of-the-art modelling has been accounted for along with the option to model the effect of the oxidation front displacement (i.e., dissolution/diffusion/re-precipitation of the hydrogen in the matrix covered by the oxide layer). It also accounts for variability in the model parameters by taking into account both the commonly used in previous models and alternatives found.

The model has been assessed through different scenarios (postulated and actual) of high burnup fuel (higher than 60 GW d/tU) irradiated in a PWR. The study allows concluding that the modelling of the oxidation front gives rise to hydride rim closer to the ones measured, both in the hydrogen concentration and the rim thickness.

Other remarks are derived from the assessment carried out:

- Hydride rim predicted with previous modelling (i.e., without the contribution of the oxidation front) is confirmed to be dense and thin, which does not match with experimental observations.
- The contribution of thermodiffusion to the hydrogen transport could be disregarded, even with the highest heat of transport (Q^*_{zr}) reported in the literature. The diffusion within the hydride phase could be disregarded too (i.e., D_δ and Q^*_δ can be considered as null).
- The reduction of the variability of the solubility limits (i.e., TSS_p and TSS_d) and the hydrogen local concentration in the hydride (H_δ), although it is not a key factor to improve the model

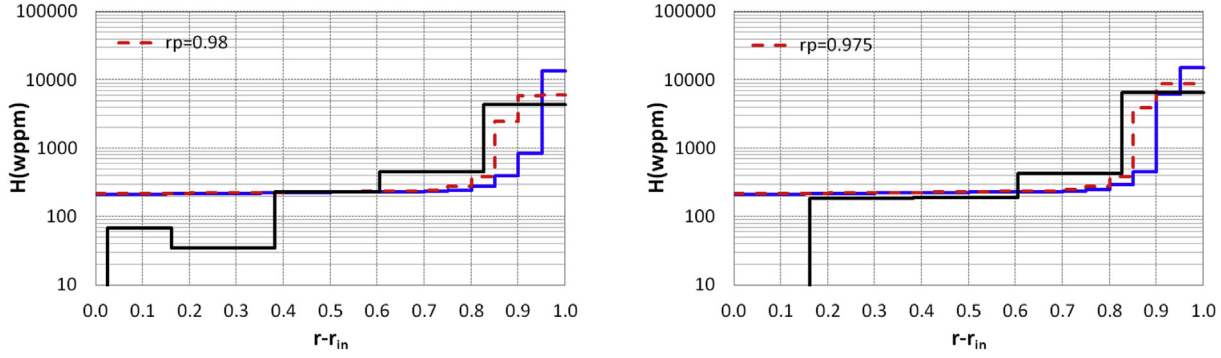

Fig. 14. EOL hydrogen radial distribution (radius normalized) for v1 (plot on the left) and v2 (plot on the right): measurements (black line), default case (blue line) and corresponding parametric case with oxidation front effect and rp_{max} (red dashed line). (For interpretation of the references to colour in this figure legend, the reader is referred to the Web version of this article.)

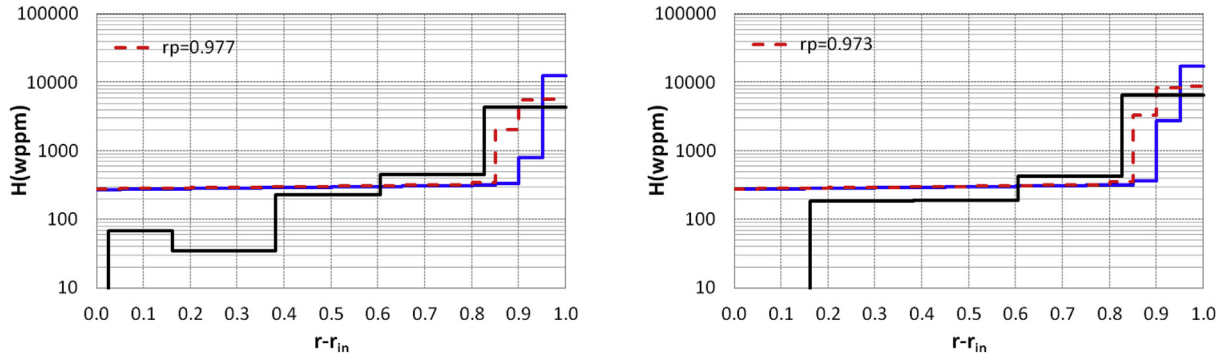

Fig. 15. EOL hydrogen radial distribution (radius normalized) for v1 (plot on the left) and v2 (plot on the right): measurements (black line), optional case (blue line) and corresponding parametric case with oxidation front effect and rp_{max} (red dashed line). (For interpretation of the references to colour in this figure legend, the reader is referred to the Web version of this article.)

accuracy, would help to increase the precision. On the contrary, the variability found in the precipitation rate parameter (k_p) hardly affects.

According to the model assessment conducted, even though it is premature to recommend any values for a best estimate given the lack of data to validate, attention should be drawn to TSSs, H_δ and, mostly, the effect of the oxidation front through rp (i.e., fraction of the precipitated hydrogen covered by the oxide that does not re-precipitate instantaneously). As for TSSs and H_δ, no net benefit has been shown to result from using what has been called "optional values", so that the default ones would be a reasonable option. Regarding rp, a low fraction of instantaneous re-precipitation is recommended (i.e., rp around 0.975). This being said, it is mandatory to stress that further investigation is required, including a critical review of the existing database, to firmly support any specific recommendation, taking into account that the above one should be considered preliminary and resulting from the work here presented.

Acknowledgment

The authors wish to thank ENRESA, particularly F.J. Fernandez, for the technical discussions held and the financial support.

References

[1] F. Schmitz, J. Papin, High burnup effects on fuel behaviour under accident conditions: the tests CABRI REP-Na, J. Nucl. Mater. 270 (1999) 55–64.
[2] NEA, Nuclear Fuel Safety Criteria Technical Review, second ed., OECD, 2012, ISBN 978-92-64-99178-1. NEA No. 7072.
[3] NRC, Cladding considerations for the transportation and storage of spent fuel, Spent Fuel Proj. Off. Interim Staff Guid. - 11, Revis 3 (2003).
[4] M.C. Billone, T.A. Burtseva, R.E. Einziger, Ductile-to-brittle transition temperature for high-burnup cladding alloys exposed to simulated drying-storage conditions, J. Nucl. Mater. 433 (2013) 431–448.
[5] H. Nagase, F. Uetsuka, Hydride morphology and hydrogen embrittlement of Zircaloy fuel cladding used in NSRR/HBO experiment, in: ANS Int. Top. Meet. Light Water React. Performance, ANS, Portland, OR, 1997, p. 677.
[6] C. Raepsaet, P. Bossis, D. Hamon, J.L. Béchade, J.C. Brachet, Quantification and local distribution of hydrogen within Zircaloy-4 PWR nuclear fuel cladding tubes at the nuclear microprobe of the Pierre Süe Laboratory from μ-ERDA, Nucl. Instruments Methods Phys. Res. Sect. B Beam Interact. with Mater. Atoms 266 (2008) 2424–2428.
[7] A. Sawatzky, Hydrogen in zircaloy-2: its distribution and heat of transport, J. Nucl. Mater. 2 (1960) 321–328.
[8] G.P. Marino, A numerical calculation of the redistribution of an interstitial solute in a thermal gradient, Nucl. Sci. Eng. 49 (1972) 93–98.
[9] O. Courty, A.T. Motta, J.D. Hales, Modeling and simulation of hydrogen behavior in Zircaloy-4 fuel cladding, J. Nucl. Mater. 452 (2014) 311–320.
[10] D.S. Stafford, Multidimensional simulations of hydrides during fuel rod life-cycle, J. Nucl. Mater. 466 (2015) 362–372.
[11] M.S. Veshchunov, V.E. Shestak, V.D. Ozrin, A new model of hydrogen redistribution in Zr alloy claddings during waterside corrosion in a temperature gradient, J. Nucl. Mater. 472 (2016) 65–75.
[12] M. Tupin, C. Bisor, P. Bossis, J. Chêne, J.L. Bechade, F. Jomard, Mechanism of corrosion of zirconium hydride and impact of precipitated hydrides on the Zircaloy-4 corrosion behaviour, Corrosion Sci. 98 (2015) 478–493.
[13] K.J. Geelhood, W.G. Lusche, P.A. Raynaud, I.E. Porter, FRAPCON-4.0: a Computer Code for the Calculation of Steady-State, Thermal-Mechanical Behavior of Oxide Fuel Rods for High Burnup, 2015. PNNL-19418, Vol. 1 Rev.2.
[14] O.F. Courty, A.T. Motta, C.J. Piotrowski, J.D. Almer, Hydride precipitation kinetics in Zircaloy-4 studied using synchrotron X-ray diffraction, J. Nucl. Mater. 461 (2015) 180–185.
[15] G. O'Donnell, H. Scott, R.O. Meyer, A New Comparative Analysis of LWR Fuel Designs, 2001. NUREG-1754.
[16] F.D. Zuzek, E. Abriata, J.P. San Martin, A. Manchester, The H_Zr (Hydrogen_ Zirconium) system, Bull. Alloy Phase Diagr 11 (1999) 385.
[17] J.S. McMinn, A. Darby, E.C. Schofield, The terminal solid solubility of hydrogen in zirconium alloys, in: 12th Int. Symp. Zr Nucl. Ind. Toronto, CA, 2000, pp. 173–195.
[18] K. Une, S. Ishimoto, Y. Etoh, K. Ito, K. Ogata, T. Baba, K. Kamimura, Y. Kobayashi, The terminal solid solubility of hydrogen in irradiated Zircaloy-2 and microscopic modeling of hydride behavior, J. Nucl. Mater. 389 (2009) 127–136.
[19] W.J. Kammenzind, B. Franklin, D.G. Peters, H.R. Duffin, Hydrogen pickup and redistribution in alpha-annealed Zircaloy-4, in: 11th Int. Symp. Zircon. Nucl. Ind. ASTM STP1295, 1997, pp. 338–369.
[20] A. Sawatzky, E. Vogt, Mathematics of the Thermal Diffusion of Hydrogen in Zircaloy-2, 1961. CRT-1049, AECL-1411.
[21] W.A. Harkness, S.D. Young, Diffusion of Hydrogen in Delta-phase Zirconium Hydride, 1965. NAA-SR-10516.
[22] H.S. Hong, S.J. Kim, K.S. Lee, Thermotransport of hydrogen in Zircaloy-4 and modified Zircaloy-4, J. Nucl. Mater. 257 (1998) 15–20.
[23] F. Feria, L.E. Herranz, Application of the BEPU methodology to assess fuel performance in dry storage, Ann. Nucl. Energy 99 (2017) 240–246.
[24] W. Sahle, PIE of CIP0–1 Father Rod: Cladding Oxide and Hydride Measurement in SEM, 2010. Studsvik Nuclear AB, N(H)-02/027 rev. 2.